

Geometrically nonlinear meshfree analysis of 3D-shell structures based on the double directors shell theory with finite rotations

Hana Mellouli², Hanen Jrad^{*2}, Mondher Wali^{1,2} and Fakhreddine Dammak²

¹ Department of Mechanical Engineering, College of Engineering, King Khalid University, Abha, Saudi Arabia

² Laboratory of Electromechanical Systems (LASEM), National Engineering School of Sfax, University of Sfax, Route de Soukra km 4, 3038 Sfax, Tunisia

(Received January 17, 2019, Revised March 26, 2019, Accepted March 29, 2019)

Abstract. In this paper, a geometrically nonlinear meshfree analysis of 3D various forms of shell structures using the double director shell theory with finite rotations is proposed. This theory is introduced in the present method to remove the shear correction factor and to improve the accuracy of transverse shear stresses with the consideration of rotational degrees of freedom. The present meshfree method is based on the radial point interpolation method (RPIM) which is employed for the construction of shape functions for a set of nodes distributed in a problem domain. Discrete system of geometrically nonlinear equilibrium equations solved with the Newton-Raphson method is obtained by incorporating these interpolations into the weak form. The accuracy of the proposed method is examined by comparing the present results with the accurate ones available in the literature and good agreements are found.

Keywords: meshfree method; geometric nonlinear analysis; 3D shell structures; double directors shell theory; finite rotations; RPIM

1. Introduction

The analysis of shell structures is of considerable interest in various areas of structural mechanics. In fact, shells are widely used in various mechanical structures, civil engineering, aerospace and naval. Two different types of shells can be distinguished by the ratio of the thickness: thin shells when the ratio is considered to be thin as $1/20$ and thick shells when the ratio is considered to be upper than $1/20$. The thin shell structures are based on the Kirchhoff-Love theory (Krysl and Belytschko 1996, Uysal 2016, Atri and Shojaei 2018, Jrad *et al.* 2018a, Mallek *et al.* 2019a) and the thick shell structures (Zhu *et al.* 2014, Zhang *et al.* 2015a, b, c) are based on the Mindlin-Reissner theory (Zhang and Liew 2016a) that requires the transverse shear strains which are related to the rotational degrees of freedom. The introduction of shear correction factors to the Reissner-Mindlin theory is considered due to the non-satisfaction of zero shear stress on top and bottom surfaces of the shell or plate. Many researchers are focused on this theory in order to highlight the effect of the shear correction factors addition. To avoid the use of shear correction factors and acquiring a parabolic distribution of the transverse shear stress, the double directors shell model DDSM is proposed by Wali *et al.* 2014, Zghal *et al.* 2017, Mallek *et al.* 2019c).

Recently, meshfree methods have been the object of attention and extensively applied to problems in plate and

shell structures, and other structural engineering problems. These methods provide an alternative to the FEMs. Unlike the last one, which rely on elements, the meshfree methods depend on points that are distributed on the problem domain and no element or other inter-relationship is required. Without elements, the meshfree methods are more applicable than the FEMs and able to overcome the difficulties that FEM encountered with the mesh such as mesh distortion in large deformation and intensive remeshing requirements especially when dealing with structures that have complex geometries and discontinuities (Liew *et al.* 2011), "Furthermore, a wide range of applications has been undertaken when the shells have been the object of several meshfree researches with linear theory (Noguchi *et al.* 2000, Sladek *et al.* 2007, Ivannikov *et al.* 2014, Wu and Liu 2016, Lei and Zhang 2018), Further, the high order shear deformation theory for linear meshfree analysis is investigated by Ferreira *et al.* (2006) and carried out later using the DDSM and the radial point interpolation method by Mellouli *et al.* (2019a), "In the same context, the modified first order shear deformation theory with linear meshfree method applied on 3D shell structures is considered by Mellouli *et al.* (2019b).

Commonly, the linear shell theories are carried out for shells undertaking small displacements under different types of loads. Nonlinear analysis of shells, however, should be investigated in the case when shell structures experience large deformations. Finite element analyzes of nonlinear shell structures have been undertaken by several researchers (Ray and Batra 2008, Kim *et al.* 2008, Li *et al.* 2010, Rama 2017, Frikha and Dammak 2017, Marinković and Rama 2017, Rezaiee *et al.* 2018, Jrad *et al.* 2018a, b,

*Corresponding author, Ph.D.,
E-mail: hanen.j@gmail.com

Rama *et al.* 2018). With the meshfree method, Liew *et al.* (2004), proposed the nonlinear analysis of plates with the mesh-free kp-Ritz method based on the first order shear deformation theory (FSDT), “Later, the element free Galerkin method is used for the nonlinear analysis of plates as presented by Qian *et al.* (2003, 2004), Belinha and Dinis (2007), Liew *et al.* (2007) and Tiago and Pimenta (2008). Zhao *et al.* (2008), carried out a geometric nonlinear analysis of plates and cylindrical shells using the FSDT. Moreover, an isogeometric-meshfree coupling approach for the nonlinear analysis of thin-shell structures is provided in Li *et al.* (2018). The high order shear deformation theory with the nonlinear analysis of plates is considered by Vu *et al.* (2018) and Nguyen *et al.* (2018), using an improved moving Kriging meshfree method. The radial point interpolation method as a meshfree method used for the analysis of 3D shell structures with the consideration of the double directors shell theory does not exist in the literature.

On the other hand, the radial point interpolation method (RPIM) is a meshfree method that combines both polynomial and radial basis functions (RBFs) (Wang and Liu 2002, Ferreira *et al.* 2005, Dinis *et al.* 2008, Kazemi *et al.* 2017) to construct the shape functions that possess the Kronecker delta property.

In this paper, we aim to extend the application of the present meshfree method to study the geometric nonlinear behavior of 3D shells with finite rotations based on the double directors theory characterized by the quadratic distribution of the shear stress. The developed meshfree model considers the radial point interpolation method for the construction of the shape functions. The zero transverse shear stress condition on top and bottom surfaces of the shell is released in this model in order to remove the C1 continuity. Numerical examples are presented in order to demonstrate the accuracy of the proposed model and to verify its validation with results reported in the literature.

2. Geometrically nonlinear meshfree formulation with the double directors shell theory (DDST)

In this section, the nonlinear formulation of the DDSM is presented. The initial and the deformed configurations of the shells are symbolized by C_0 and C_t , respectively. Capital letters (respectively lowercase letters) are referred to quantities of configuration C_0 (respectively C_t), “Vectors and tensors will be denoted by bold letters.

2.1 Initial and deformed configurations of the displacement field

To describe the 3D shell geometry, the Cartesian coordinate system (E_i), $i = 1, 2, 3$, is adopted. All material points of the shell are defined using the curvilinear coordinates $\xi = (\xi^1, \xi^2, \xi^3 = z)$. The position vectors of any material point (I), whose normal projection on mid-surface is the material point (J), in the initial state C_0 , are expressed using the director unit vector \mathbf{D} and the thickness of the structure h , as

$$\mathbf{X}_I(\xi^1, \xi^2, z) = \mathbf{X}_J(\xi^1, \xi^2) + z\mathbf{D}(\xi^1, \xi^2), \quad z \in \left[-\frac{h}{2}, \frac{h}{2}\right] \quad (1)$$

The base vectors, in the initial state C_0 are defined as

$$\mathbf{G}_\alpha = \mathbf{A}_\alpha + z\mathbf{D}_{,\alpha}, \quad \mathbf{G}_3 = \mathbf{D}, \quad \alpha = 1, 2 \quad (2)$$

In the deformed configuration, the position vector of the point q is expressed, considering the hypothesis of the DDSM, Wali *et al.* (2014), as

$$\mathbf{x}_q(\xi^1, \xi^2, z) = \mathbf{x}_p(\xi^1, \xi^2) + f_1(z)\mathbf{d}_1(\xi^1, \xi^2) + f_2(z)\mathbf{d}_2(\xi^1, \xi^2) \quad (3)$$

In order to satisfy the quadratic distribution of the shear stress, the expressions of $f_1(z)$ and $f_2(z)$ are defined, using the DDSM, as

$$f_1(z) = z - f_2(z), \quad f_2(z) = \frac{4z^3}{3h^2} \quad (4)$$

In the deformed state C_t , the base vectors are defined as follows

$$\begin{aligned} \mathbf{g}_\alpha &= \mathbf{a}_\alpha + f_1(z)\mathbf{d}_{1,\alpha} + f_2(z)\mathbf{d}_{2,\alpha}; \\ \mathbf{g}_3 &= f_1'(z)\mathbf{d}_1 + f_2'(z)\mathbf{d}_2 \end{aligned} \quad (5)$$

With some approximations, the metric tensor can be written as

$$\begin{aligned} g_{ij} &= \mathbf{g}_i \cdot \mathbf{g}_j, \quad \alpha, \beta = 1, 2 \\ \begin{cases} g_{\alpha\beta} \approx a_{\alpha\beta} + f_1(z)b_{\alpha\beta}^1 + f_2(z)b_{\alpha\beta}^2 + o(z^2) \\ g_{\alpha 3} \approx f_1'(z)c_\alpha^1 + f_2'(z)c_\alpha^2 + o(z) \end{cases} \end{aligned} \quad (6)$$

in which $a_{\alpha\beta}$ represent the covariant metric surface, $b_{\alpha\beta}^k$ ($k = 1, 2$) denote the curvature tensors and c_α^k ($k = 1, 2$) symbolize the shear tensor. Assuming $\mathbf{d}_1, \mathbf{d}_1 \approx \mathbf{d}_2, \mathbf{d}_2 \approx \mathbf{d}_1, \mathbf{d}_2$, the following components can be written as

$$\begin{cases} a_{\alpha\beta} = \mathbf{a}_\alpha \cdot \mathbf{a}_\beta \\ b_{\alpha\beta}^k = \mathbf{a}_\alpha \cdot \mathbf{d}_{k,\beta} + \mathbf{a}_\beta \cdot \mathbf{d}_{k,\alpha}, \quad k = 1, 2 \\ c_\alpha^k = \mathbf{a}_\alpha \cdot \mathbf{d}_k \end{cases} \quad (7)$$

2.2 The strain field

To describe the 3D shell geometry, the Cartesian coordinate system (E_i), $i = 1, 2, 3$.

The Lagrangian strain \mathbf{E} is expressed, using the kinematic assumption Eq. (6), as

$$\begin{aligned} \mathbf{E} &= \frac{1}{2}(\mathbf{g} - \mathbf{G}), \\ E_{ij} &= \frac{1}{2}(\mathbf{g}_{ij} - \mathbf{G}_{ij}), \quad \begin{cases} E_{\alpha\beta} = e_{\alpha\beta} + f_1(z)\chi_{\alpha\beta}^1 + f_2(z)\chi_{\alpha\beta}^2 \\ 2E_{\alpha 3} = f_1'(z)\gamma_\alpha^1 + f_2'(z)\gamma_\alpha^2 \end{cases} \end{aligned} \quad (8)$$

where $e_{\alpha\beta}$, $\chi_{\alpha\beta}^k$ and γ_α^k denote respectively the membrane, the bending and the shear strains.

The membrane strains $e_{\alpha\beta}$, the bending strains $\chi_{\alpha\beta}^k$ and the shear strains γ_α^k can be computed as

$$\begin{cases} e_{\alpha\beta} = \frac{1}{2}(a_{\alpha\beta} - A_{\alpha\beta}) \\ \chi_{\alpha\beta}^k = \frac{1}{2}(b_{\alpha\beta} - B_{\alpha\beta}), \\ \gamma_\alpha^k = c_\alpha - C_\alpha \end{cases} \quad k = 1, 2 \quad (9)$$

The membrane, bending and shear strains can be expressed, in matrix notation, as

$$\mathbf{e} = \begin{bmatrix} e_{11} \\ e_{22} \\ 2e_{12} \end{bmatrix}, \quad \boldsymbol{\chi}^k = \begin{bmatrix} \chi_{11}^k \\ \chi_{22}^k \\ 2\chi_{12}^k \end{bmatrix}, \quad \boldsymbol{\gamma}^k = \begin{bmatrix} \gamma_1^k \\ \gamma_2^k \end{bmatrix}, \quad k = 1, 2 \quad (10)$$

The virtual strains are formulated using Eq. (10) as

$$\begin{cases} \delta e_{\alpha\beta} = \frac{1}{2}(\mathbf{a}_\alpha \cdot \delta \mathbf{x}_\beta + \mathbf{a}_\beta \cdot \delta \mathbf{x}_\alpha) \\ \delta \chi_{\alpha\beta}^k = \frac{1}{2}(\mathbf{a}_\alpha \cdot \delta \mathbf{d}_{k\beta} + \mathbf{a}_\beta \cdot \delta \mathbf{d}_{k\alpha} + \delta \mathbf{x}_{\alpha} \cdot \mathbf{d}_{k\beta} + \delta \mathbf{x}_{\beta} \cdot \mathbf{d}_{k\alpha}), \\ \delta \gamma_\alpha^k = \mathbf{a}_\alpha \cdot \delta \mathbf{d}_k + \delta \mathbf{x}_\alpha \cdot \mathbf{d}_k \end{cases} \quad k = 1, 2 \quad (11)$$

These particles are rewritten in matrix form as

$$\begin{aligned} \delta \mathbf{e} &= \mathbf{B}_m \cdot \delta \mathbf{x}, \quad \delta \boldsymbol{\chi}^k = \mathbf{B}_{km} \delta \mathbf{x} + \mathbf{B}_{kb} \delta \mathbf{d}_k, \\ \delta \boldsymbol{\gamma}^k &= \mathbf{B}_{ksm} \delta \mathbf{x} + \mathbf{B}_{ksb} \delta \mathbf{d}_k \end{aligned}, \quad k = 1, 2 \quad (12)$$

where matrix differential operators, relative to the deformed state C_t , are given in Box 1.

Box 1: Matrix differential operators

$$\begin{aligned} \mathbf{B}_m &= \begin{bmatrix} \mathbf{a}_1^T \frac{\partial}{\partial \xi^1} \\ \mathbf{a}_2^T \frac{\partial}{\partial \xi^2} \\ \mathbf{a}_1^T \frac{\partial}{\partial \xi^2} + \mathbf{a}_2^T \frac{\partial}{\partial \xi^1} \end{bmatrix}, \quad \mathbf{B}_{km} = \begin{bmatrix} \mathbf{d}_{k,1}^T \frac{\partial}{\partial \xi^1} \\ \mathbf{d}_{k,2}^T \frac{\partial}{\partial \xi^2} \\ \mathbf{d}_{k,1}^T \frac{\partial}{\partial \xi^2} + \mathbf{d}_{k,2}^T \frac{\partial}{\partial \xi^1} \end{bmatrix}, \quad \mathbf{B}_{kb} = \mathbf{B}_m \\ \mathbf{B}_{ksm} &= \begin{bmatrix} \mathbf{d}_k^T \frac{\partial}{\partial \xi^1} \\ \mathbf{d}_k^T \frac{\partial}{\partial \xi^2} \end{bmatrix}, \quad \mathbf{B}_{ksb} = \begin{bmatrix} \mathbf{a}_1^T \\ \mathbf{a}_2^T \end{bmatrix}, \quad k = 1, 2 \end{aligned} \quad (12)$$

2.3 The weak form

The weak form of equilibrium equations, used for the numerical solutions with the meshfree method, is given, using the contravariant components of the second Piola-Kirchhoff stress tensor S^{ij} , the covariant components of the virtual Green-Lagrange strain tensor δE_{ij} , the shell volume structure in the initial configuration dV and the external virtual work G_{ext} , as

$$G = \int_V S^{ij} \delta E_{ij} dV - G_{ext} = 0 \quad (13)$$

The membrane N , bending \mathbf{M}^k and shear \mathbf{T}^k stress resultants, can be written, respectively, in matrix form, as

$$\mathbf{N} = \begin{bmatrix} N^{11} \\ N^{22} \\ N^{12} \end{bmatrix}, \quad \mathbf{M}_k = \begin{bmatrix} M_k^{11} \\ M_k^{22} \\ M_k^{12} \end{bmatrix}, \quad \mathbf{T}_k = \begin{bmatrix} T_k^1 \\ T_k^2 \end{bmatrix}, \quad k = 1, 2 \quad (14)$$

Where components are defined as follows, $\alpha, \beta = 1, 2$ and $k = 1, 2$

$$\begin{aligned} N^{\alpha\beta} &= \int_{-h/2}^{h/2} S^{\alpha\beta} \sqrt{\frac{G}{A}} dz, \quad M_k^{\alpha\beta} = \int_{-h/2}^{h/2} f_k(z) S^{\alpha\beta} \sqrt{\frac{G}{A}} dz, \\ T_k^\alpha &= \int_{-h/2}^{h/2} f_k'(z) S^{\alpha 3} \sqrt{\frac{G}{A}} dz \end{aligned} \quad (15)$$

The weak form can be rewritten, using the components of the stress resultants defined in Eq. (14) and the shell strains $\delta \mathbf{e}$, $\delta \boldsymbol{\chi}^k$ and $\delta \boldsymbol{\gamma}^k$ represented in Eq. (12), as

$$G = \int_A \left(\mathbf{N} \cdot \delta \mathbf{e} + \sum_{k=1}^2 (\mathbf{M}_k \cdot \delta \boldsymbol{\chi}^k + \mathbf{T}_k \cdot \delta \boldsymbol{\gamma}^k) \right) dA - G_{ext} = 0 \quad (16)$$

It should be noted that the condition of zero shear stress on top and bottom surfaces of the shell structure is released in the present formulation in order to get rid of the difficulties caused by the satisfaction of the C^1 continuity.

The weak form of the equilibrium equation can be rewritten as

$$G(\boldsymbol{\Phi}, \delta \boldsymbol{\Phi}) = \int_A \delta \boldsymbol{\Sigma}^T \cdot \mathbf{R} dA - G_{ext}(\boldsymbol{\Phi}, \delta \boldsymbol{\Phi}) = 0 \quad (17)$$

Where the generalized resultants of stress \mathbf{R} and strain $\boldsymbol{\Sigma}$ are defined as

$$\mathbf{R} = \begin{bmatrix} N \\ \mathbf{M}_1 \\ \mathbf{M}_2 \\ \mathbf{T}_1 \\ \mathbf{T}_2 \end{bmatrix}_{13 \times 1}, \quad \boldsymbol{\Sigma} = \begin{bmatrix} \mathbf{e} \\ \boldsymbol{\chi}^1 \\ \boldsymbol{\chi}^2 \\ \boldsymbol{\gamma}^1 \\ \boldsymbol{\gamma}^2 \end{bmatrix}_{13 \times 1} \quad (18)$$

2.4 Meshfree approximation of high order deformation shell structures

Since there is no mesh of elements in the meshfree method, the shape functions are constructed using only nodes within overlapping domains named as support domains. A support domain of a point X determines the number of nodes to be used to support or approximate the function value at X , allowing a richer approximation and avoiding any artificial discontinuity in the field. The meshfree method concepts are described in this section.

2.4.1 The radial point interpolation method (RPIM)

The RPIM which represents an interpolator meshfree method that combines a radial basis function $R^l(X)$ with a

polynomial basis function $P^J(X)$, is described in this section. For a point of interest $X = (x, y)$ presented in a support domain, the approximation of the displacement vector is expressed, using a_1 and b_j the non-constants coefficients of $R^I(X)$ and $P^J(X)$, as

$$U(X) = \sum_{I=1}^N R^I(X) a_1 + \sum_{J=1}^M P^J(X) b_j = \mathbf{R}^T(X) \mathbf{a} + \mathbf{P}^T(X) \mathbf{b} \quad (19)$$

N denotes the number of nodes presented in a support domain and M is the number of monomial terms with the condition of $M < N$. For example in this study, a quadratic basis requires $M = 6$ as presented in Eq. (20).

$$\mathbf{P}^T(X) = [1, x, y, x^2, xy, y^2] \quad (20)$$

The displacement vector can be rewritten, in matrix notation using the radial moment matrix \mathbf{R} , the polynomial moment matrix \mathbf{P} , the vector of coefficients for RBFs \mathbf{a} and the vector of coefficients for polynomial matrix \mathbf{b} , as

$$\begin{aligned} \mathbf{U} &= \mathbf{R}\mathbf{a} + \mathbf{P}\mathbf{b} \\ \mathbf{R} &= \begin{bmatrix} R_1(X_1) & R_2(X_1) & \dots & R_N(X_1) \\ R_1(X_2) & R_2(X_2) & \dots & R_N(X_2) \\ \dots & \dots & \dots & \dots \\ R_1(X_N) & R_2(X_N) & \dots & R_N(X_N) \end{bmatrix}_{(N \times N)} \\ \mathbf{P}^T &= \begin{bmatrix} 1 & x_1 & y_1 & \dots & 1 \\ 1 & x_2 & y_2 & \dots & 1 \\ \dots & \dots & \dots & \dots & \dots \\ 1 & x_N & y_N & \dots & 1 \end{bmatrix}_{(M \times N)} \\ \mathbf{a}^T &= [a_1 \ a_2 \ \dots \ a_N], \quad \mathbf{b}^T = [b_1 \ b_2 \ \dots \ b_M] \end{aligned} \quad (21)$$

The frequently used types of radial basis functions RBFs, Liu and Gu (2005), are presented in Table 1.

c and q represent the two shape parameters characterizing the RBFs and $\|X_j - X\|$ is the Euclidean norm specifying the distance between a defining-point X_j ($j = 1, \dots, N$) and a point of interest X . The advantage of an RBFs is that it requires only the distance between 2 nodes contrarily to the finite element method. The shape parameter c specifies the average nodal spacing for the total nodes locating in the local support domain and in order to reach the accurate results, the optimal shape parameter q is equal to $q = 1.03$. Eq. (19) presents total $N+M$ variables. So, in order to obtain square matrix and guarantee unique approximation, Liu and Gu (2005), an M polynomial equations can be added verifying the relation presented at

Table 1 Frequently used types of RBFs

Multiquadrics	$R^I(X) = (\ X_j - X\ ^2 + c^2)^q$
Gaussians	$R^I(X) = \exp(-c^2\ X_j - X\ ^2)$

Eq. (22).

$$\sum_{I=1}^N P_j(X_I) a_1 = 0 \quad (22)$$

The combination of Eqs. (19) and (22) leads to the following set of matrix form equations using the complete moment matrix \mathbf{G}

$$\begin{bmatrix} \mathbf{R} & \mathbf{P} \\ \mathbf{P}^T & \mathbf{0} \end{bmatrix} \begin{bmatrix} \mathbf{a} \\ \mathbf{b} \end{bmatrix} = \begin{bmatrix} \mathbf{U} \\ \mathbf{0} \end{bmatrix} \Leftrightarrow \mathbf{G} \begin{bmatrix} \mathbf{a} \\ \mathbf{b} \end{bmatrix} = \begin{bmatrix} \mathbf{U} \\ \mathbf{0} \end{bmatrix} \quad (23)$$

It will be guaranteed the symmetry of the matrix \mathbf{G} from the symmetry of the matrix \mathbf{R} and a unique solution is reached if the inverse of the matrix \mathbf{R} exists.

Using the moment matrix \mathbf{G} and the RPIM shape function defined in Eq. (25), the displacement vector is given as

$$\mathbf{U}(X) = [\mathbf{R}^T(X) \ \mathbf{P}^T(X)] \mathbf{G}^{-1} \begin{bmatrix} \mathbf{U} \\ \mathbf{0} \end{bmatrix} = \boldsymbol{\phi}^T(X) \begin{bmatrix} \mathbf{U} \\ \mathbf{0} \end{bmatrix} \quad (24)$$

$$\begin{aligned} \boldsymbol{\phi}^T(X) &= [\mathbf{R}^T(X) \ \mathbf{P}^T(X)] \mathbf{G}^{-1} \\ &= [\phi_1(X) \ \phi_2(X) \ \dots \ \phi_N(X)] \end{aligned} \quad (25)$$

Using the RPIM, the displacement vector \mathbf{U} , defined as $\mathbf{U} = \mathbf{x}_p - \mathbf{x}_p$, its incremental variation $\Delta \mathbf{U}$ and the first and second director vectors d_1 and d_2 are approximated by

$$\begin{aligned} \mathbf{U} &= \sum_{I=1}^N \phi^I \mathbf{u}_I, \Delta \mathbf{U} = \sum_{I=1}^N \phi^I \Delta \mathbf{u}_I, \delta d_1 = \sum_{I=1}^N \phi^I \delta d_{1I}, \\ \Delta d_1 &= \sum_{I=1}^N \phi^I \Delta d_{1I}, \delta d_2 = \sum_{I=1}^N \phi^I \delta d_{2I}, \Delta d_2 = \sum_{I=1}^N \phi^I \Delta d_{2I} \end{aligned} \quad (26)$$

where N represents the nodes number.

2.4.2 Local Cartesian system

Considering $\mathbf{n}^0 = \frac{\mathbf{A}_1 \wedge \mathbf{A}_2}{\|\mathbf{A}_1 \wedge \mathbf{A}_2\|}$ the normal field to the mid-surface in the initial state C_0 , as illustrated in Fig. 1. A local Cartesian system with the base vectors $\{\mathbf{n}_1^0, \mathbf{n}_2^0, \mathbf{n}^0\}$, can be defined using the orthogonal transformation. Therefore, the Jacobian transformation \mathbf{J} from the basis $\{\mathbf{n}_1^0, \mathbf{n}_2^0\}$ to $\{\mathbf{A}_1, \mathbf{A}_2\}$ can be expressed as

$$\mathbf{J} = \begin{bmatrix} \mathbf{n}_1^0 \cdot \mathbf{A}_1 & \mathbf{n}_2^0 \cdot \mathbf{A}_1 \\ \mathbf{n}_1^0 \cdot \mathbf{A}_2 & \mathbf{n}_2^0 \cdot \mathbf{A}_2 \end{bmatrix} \quad (27)$$

The derivatives of the shape functions need to be reconstructed, since the formulation is developed in local Cartesian coordinates, as mentioned in Eq. (28).

$$\begin{bmatrix} \frac{\partial}{\partial x} \\ \frac{\partial}{\partial y} \end{bmatrix} = [\mathbf{J}]^{-1} \begin{bmatrix} \frac{\partial}{\partial \xi} \\ \frac{\partial}{\partial \eta} \end{bmatrix} \quad (28)$$

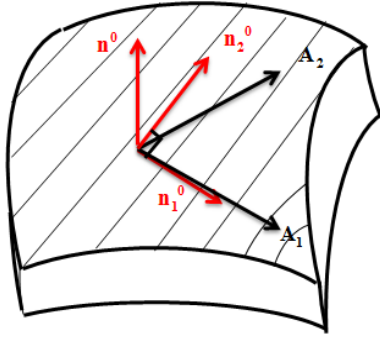


Fig. 1 The system coordinates of the shell structure

To model any arbitrary geometry shape (cylindrical, spherical... structures), a transformation from local Cartesian space, related to arbitrary complex surface, to a parametric space is required.

The local Cartesian basis of the deformed configuration is given by

$$\mathbf{n}_1 = \sum_{I=1}^N \varphi_{,1}^{-I} (\mathbf{X} + \mathbf{U})_I, \quad \mathbf{n}_2 = \sum_{I=1}^N \varphi_{,2}^{-I} (\mathbf{X} + \mathbf{U})_I \quad (29)$$

In what follows, membrane strain field \mathbf{e} , first and second bending strain field χ^1 and χ^2 , first and second transverse shear strain field γ^1 and γ^2 are derived by means of the RPIM.

2.4.3 Membrane strain field

The strain-displacement relation for the shell membrane is expressed as

$$\delta \mathbf{e} = \mathbf{B}_m \cdot \delta \Phi \quad (30)$$

For all nodes N locating in the support domain, Φ presents the discrete displacement approximation and \mathbf{B}_m is the membrane strain-displacement operator expressed as

$$\mathbf{B}_m^I = \begin{bmatrix} \mathbf{B}_{mm}^I & \mathbf{0} & \mathbf{0} \end{bmatrix}, \quad \mathbf{B}_{mm}^I = \begin{bmatrix} \mathbf{n}_1^T \varphi_{,1}^{-I} \\ \mathbf{n}_2^T \varphi_{,2}^{-I} \\ \mathbf{n}_1^T \varphi_{,2}^{-I} + \mathbf{n}_2^T \varphi_{,1}^{-I} \end{bmatrix} \quad (31)$$

2.4.4 First and second bending strain field

For the first and second bending part, the strain-displacement relations are given by

$$\delta \chi^1 = \mathbf{B}_1 \cdot \delta \Phi \quad (32)$$

$$\delta \chi^2 = \mathbf{B}_2 \cdot \delta \Phi \quad (33)$$

where \mathbf{B}_1 and \mathbf{B}_2 define respectively the discrete first and second bending strain-displacement operator.

$$\mathbf{B}_1^I = \begin{bmatrix} \mathbf{B}_{1m}^I & \mathbf{B}_{1b}^I & \mathbf{0} \end{bmatrix}, \quad \mathbf{B}_{1m}^I = \begin{bmatrix} \mathbf{d}_{1,1}^T \varphi_{,1}^{-I} \\ \mathbf{d}_{1,2}^T \varphi_{,2}^{-I} \\ \mathbf{d}_{1,1}^T \varphi_{,2}^{-I} + \mathbf{d}_{1,2}^T \varphi_{,1}^{-I} \end{bmatrix}, \quad (34)$$

$$\mathbf{B}_{1b}^I = \begin{bmatrix} \mathbf{n}_1^T \varphi_{,1}^{-I} \\ \mathbf{n}_2^T \varphi_{,2}^{-I} \\ \mathbf{n}_1^T \varphi_{,2}^{-I} + \mathbf{n}_2^T \varphi_{,1}^{-I} \end{bmatrix} \quad (34)$$

$$\mathbf{B}_2^I = \begin{bmatrix} \mathbf{B}_{2m}^I & \mathbf{0} & \mathbf{B}_{2b}^I \end{bmatrix}, \quad \mathbf{B}_{2m}^I = \begin{bmatrix} \mathbf{d}_{2,1}^T \varphi_{,1}^{-I} \\ \mathbf{d}_{2,2}^T \varphi_{,2}^{-I} \\ \mathbf{d}_{2,1}^T \varphi_{,2}^{-I} + \mathbf{d}_{2,2}^T \varphi_{,1}^{-I} \end{bmatrix}, \quad (35)$$

$$\mathbf{B}_{2b}^I = \begin{bmatrix} \mathbf{n}_1^T \varphi_{,1}^{-I} \\ \mathbf{n}_2^T \varphi_{,2}^{-I} \\ \mathbf{n}_1^T \varphi_{,2}^{-I} + \mathbf{n}_2^T \varphi_{,1}^{-I} \end{bmatrix}$$

where $\mathbf{d}_{1,k} = \sum_{I=1}^N \varphi_{,k}^{-I} \mathbf{d}_{1I}$, $\mathbf{d}_{2,k} = \sum_{I=1}^N \varphi_{,k}^{-I} \mathbf{d}_{2I}$, $k=1,2$ and N : the nodes' number existing in the support domain.

2.4.5 First and second shear strain field

For the first and second transverse shear part, the strain-displacement relations are expressed as

$$\delta \gamma^1 = \mathbf{B}_{s1} \cdot \delta \Phi \quad (36)$$

$$\delta \gamma^2 = \mathbf{B}_{s2} \cdot \delta \Phi \quad (37)$$

where \mathbf{B}_{s1} and \mathbf{B}_{s2} represent respectively the discrete first and second transverse shear strain-displacement operator

$$\mathbf{B}_{s1}^I = \begin{bmatrix} \mathbf{B}_{1sm}^I & \mathbf{B}_{1sb}^I & \mathbf{0} \end{bmatrix}, \quad \mathbf{B}_{1sm}^I = \begin{bmatrix} \mathbf{d}_1^T \varphi_{,1}^{-I} \\ \mathbf{d}_1^T \varphi_{,2}^{-I} \end{bmatrix}, \quad \mathbf{B}_{1sb}^I = \begin{bmatrix} \mathbf{n}_1^T \varphi_{,1}^{-I} \\ \mathbf{n}_1^T \varphi_{,2}^{-I} \end{bmatrix} \quad (38)$$

$$\mathbf{B}_{s2}^I = \begin{bmatrix} \mathbf{B}_{2sm}^I & \mathbf{0} & \mathbf{B}_{2sb}^I \end{bmatrix}, \quad \mathbf{B}_{2sm}^I = \begin{bmatrix} \mathbf{d}_2^T \varphi_{,1}^{-I} \\ \mathbf{d}_2^T \varphi_{,2}^{-I} \end{bmatrix}, \quad \mathbf{B}_{2sb}^I = \begin{bmatrix} \mathbf{n}_1^T \varphi_{,1}^{-I} \\ \mathbf{n}_1^T \varphi_{,2}^{-I} \end{bmatrix} \quad (39)$$

2.5 Linearization of the weak form

The expressions of the virtual and incremental generalized strains are presented as follows

$$\delta \Sigma = \mathbf{B} \cdot \delta \Phi, \quad \Delta \Sigma = \mathbf{B} \cdot \Delta \Phi \quad (40)$$

where \mathbf{B} is given as

$$\mathbf{B} = \begin{bmatrix} \mathbf{B}_m \\ \mathbf{B}_1 \\ \mathbf{B}_2 \\ \mathbf{B}_{s_1} \\ \mathbf{B}_{s_2} \end{bmatrix} \quad (41)$$

The internal virtual work, using Eq. (17), becomes

$$\mathbf{G}_{int} = \delta \Phi^T \int_A (\mathbf{B}^T \cdot \mathbf{R}) dA \quad (42)$$

The nonlinear shell problem, solved by the Newton iterative procedure, is defined using Eq. (17). For the Newton solution procedure, the consistent tangent operator can be established using the weak form directional derivatives in the direction of the increment $\Delta \Phi = (\Delta U, \Delta \mathbf{d}_1, \Delta \mathbf{d}_2)$. It is practical to split the tangent operator into geometric and material parts, denoted by $D_G \mathbf{G} \cdot \Delta \Phi$ and $D_M \mathbf{G} \cdot \Delta \Phi$, respectively

$$D\mathbf{G} \cdot \Delta \Phi = D_G \mathbf{G} \cdot \Delta \Phi + D_M \mathbf{G} \cdot \Delta \Phi \quad (43)$$

2.5.1 Material part

The material part of the tangent operator, resulting from the variation in the stresses resultant, takes the following form

$$D_M \mathbf{G} \cdot \Delta \Phi = \int_A \delta \Sigma^T \cdot \Delta \mathbf{R} dA = \int_A \delta \Sigma^T \cdot \mathbf{H}_T \cdot \Delta \Sigma dA \quad (44)$$

The material tangent modulus is given as

$$\Delta \mathbf{R} = \mathbf{H}_T \Delta \Sigma \quad (45)$$

where the material tangent modulus is defined as

$$\mathbf{H}_T = \begin{bmatrix} H_{11} & H_{12} & H_{13} & H_{14} & H_{15} \\ & H_{22} & H_{23} & H_{24} & H_{25} \\ & & H_{33} & H_{34} & H_{35} \\ & & & H_{44} & H_{45} \\ sym & & & & H_{55} \end{bmatrix} \quad (46)$$

$$(\mathbf{H}_{11}, \mathbf{H}_{12}, \mathbf{H}_{13}, \mathbf{H}_{22}, \mathbf{H}_{23}, \mathbf{H}_{33}) = \int_{-h/2}^{h/2} (1, f_1, f_2, f_1^2, f_1 f_2, f_2^2) \mathbf{H} dz \quad (47)$$

$$(\mathbf{H}_{14}, \mathbf{H}_{24}, \mathbf{H}_{34}, \mathbf{H}_{44}, \mathbf{H}_{54}) = \int_{-h/2}^{h/2} (0, 0, 0, (f_1')^2, f_1' f_2') \mathbf{H}_r dz \quad (48)$$

$$(\mathbf{H}_{15}, \mathbf{H}_{25}, \mathbf{H}_{35}, \mathbf{H}_{45}, \mathbf{H}_{55}) = \int_{-h/2}^{h/2} (0, 0, 0, f_1' f_2', (f_2')^2) \mathbf{H}_r dz \quad (49)$$

where \mathbf{H} and \mathbf{H}_r are respectively the in plane and out-of-plane linear elastic sub-matrices, given by

$$\mathbf{H} = \frac{E(z)}{1-\nu^2(z)} \begin{bmatrix} 1 & \nu(z) & 0 \\ \nu(z) & 1 & 0 \\ 0 & 0 & (1-\nu(z))/2 \end{bmatrix}, \quad (50)$$

$$\mathbf{H}_r = \frac{E(z)}{2(1+\nu(z))} \begin{bmatrix} 1 & 0 \\ 0 & 1 \end{bmatrix}$$

Using Eqs. (44) and (45), the material tangent operator is expressed as

$$\mathbf{K}_m = \int_A (\mathbf{B}^T \cdot \mathbf{H}_T \cdot \mathbf{B}) dA \quad (51)$$

2.5.2 Geometrical part

The geometric part is developed, from the variation of the virtual strains using the stresses resultant constant, as

$$D_G \mathbf{G} \cdot \Delta \Phi = \int_A (\Delta \delta \Sigma^T \cdot \mathbf{R}) dA \quad (52)$$

Eq. (52) can be decomposed in membrane ($D_G \mathbf{G}_m$), bending ($D_G \mathbf{G}_{b_1}$, $D_G \mathbf{G}_{b_2}$) and shear ($D_G \mathbf{G}_{s_1}$, $D_G \mathbf{G}_{s_2}$) terms as follows

$$D_G \mathbf{G} \cdot \Delta \Phi = D_G \mathbf{G}_m \cdot \Delta \Phi + D_G \mathbf{G}_{b_1} \cdot \Delta \Phi + D_G \mathbf{G}_{b_2} \cdot \Delta \Phi + D_G \mathbf{G}_{s_1} \cdot \Delta \Phi + D_G \mathbf{G}_{s_2} \cdot \Delta \Phi \quad (53)$$

The geometric tangent operator, based on Eq. (53), becomes in matrix form as

$$D_G \mathbf{G} \cdot \Delta \Phi = \delta \Phi^T (\mathbf{K}_{G_m} + \mathbf{K}_{G_{b_1}} + \mathbf{K}_{G_{b_2}} + \mathbf{K}_{G_{s_1}} + \mathbf{K}_{G_{s_2}}) \Delta \Phi \quad (54)$$

Membrane, bending and shear terms can be added to the geometric tangent operator \mathbf{K}_G as

$$D_G \mathbf{G} \cdot \Delta \Phi = \delta \Phi^T \mathbf{K}_G \Delta \Phi \quad (55)$$

where \mathbf{K}_G is symmetric.

The global geometric tangent operator is detailed in Appendix A.

2.6 Nodal transformation

The expressions of the virtual and incremental generalized strains are presented as follows:

The variation of the directors $\delta \mathbf{d}_{kl}$, $k = 1, 2$ and their derivatives $\delta \mathbf{d}_{kl,a}$, $k = 1, 2$ is expressed, for a node "I" presented in the support domain with a spatial description, as

$$\delta \mathbf{d}_{kl} = \delta \boldsymbol{\theta}_{kl} \wedge \mathbf{d}_{kl} = \mathbf{A}_{kl} \delta \boldsymbol{\theta}_{kl}, \quad \bar{\mathbf{A}}_{kl} = -\tilde{\mathbf{d}}_{kl}, \quad k = 1, 2 \quad (56)$$

where $\tilde{\mathbf{d}}_{kl}$ is the skew-symmetric tensor such that $\tilde{\mathbf{d}}_{kl} \mathbf{d}_{kl} = 0$, or in material description

Table 2 The nodal updates

The updating displacement vector	$\mathbf{U}_I^{k+1} = \mathbf{U}_I^k + \Delta \mathbf{U}$
The updating rotations	$\Delta \mathbf{d} = \Delta \boldsymbol{\theta} \bar{\mathbf{A}}_I^k,$
	$\mathbf{d}_I^{k+1} = \cos(\Delta \mathbf{d}) \mathbf{d}_I^k + \frac{\sin(\Delta \mathbf{d})}{\Delta \mathbf{d}} \Delta \mathbf{d}, \Delta \mathbf{d} = \ \Delta \mathbf{d}\ ,$
	$\bar{\mathbf{A}}_I^{k+1} = \exp(\bar{\Delta \boldsymbol{\theta}}) \bar{\mathbf{A}}_I^k,$
	$\Delta \boldsymbol{\theta} = \mathbf{d}_I^k \wedge \Delta \mathbf{d}$

$$\begin{aligned}\delta \mathbf{d}_{kl} &= \mathbf{Q}_{kl} \delta \bar{\boldsymbol{\Theta}}_{kl} \mathbf{E}_3 = \bar{\mathbf{A}}_{kl} \delta \bar{\boldsymbol{\Theta}}_{kl}, \\ \bar{\mathbf{A}}_{kl} &= \mathbf{Q}_{kl} \bar{\mathbf{E}}_3, \quad k = 1, 2\end{aligned}\quad (57)$$

where $\mathbf{d}_{kl} = \mathbf{Q}_{kl} \mathbf{E}_3$, $\mathbf{E}_3 = [0 \ 0 \ 1]^T$ and $\mathbf{Q}_{kl} = [\mathbf{t}_{1kl} \ \mathbf{t}_{2kl} \ \mathbf{t}_{3kl}]$ in which $[\mathbf{t}_{1kl} \ \mathbf{t}_{2kl} \ \mathbf{t}_{3kl}]$ are the orthogonal base of the matrix \mathbf{Q}_{kl} (Mallek *et al.* 2019b), “A spatial description defines the shell problem with 9 DOF/node while the material description needs 7 DOF/node.

For a node “I” locating in the support domain, the generalized displacement vector $\boldsymbol{\Phi}_I = (\mathbf{U}_I, \mathbf{d}_{1I}, \mathbf{d}_{2I})$ is related to the nodal variables vector $\boldsymbol{\Gamma}_I = (\mathbf{U}_I, \boldsymbol{\Theta}_{1I}, \boldsymbol{\Theta}_{2I})$ as follows

$$\delta \boldsymbol{\Phi}_I = \boldsymbol{\Pi}_I \delta \boldsymbol{\Gamma}_I, \quad \boldsymbol{\Pi}_I = \begin{bmatrix} \mathbf{I} & \mathbf{0} & \mathbf{0} \\ \mathbf{0} & \bar{\mathbf{A}}_{1I} & \mathbf{0} \\ \mathbf{0} & \mathbf{0} & \bar{\mathbf{A}}_{2I} \end{bmatrix} \quad (58)$$

2.7 Nodal updates

Considering large deformations of the shell structures, the generalized displacement vector at node ‘I’ is updated as seen in Table 2.

After the nodal transformation, the nodal updates and using Eqs. (17), (40) and (45), the internal virtual work becomes

$$\begin{aligned}G_{int} &= \int_A \delta \boldsymbol{\Sigma}^T \cdot \mathbf{R} dA = \delta \boldsymbol{\Gamma}^T \mathbf{K} \boldsymbol{\Gamma}, \\ K_{IJ} &= \int_A \boldsymbol{\Pi}_I^T \mathbf{B}_I^T \mathbf{H}_T \mathbf{B}_J \boldsymbol{\Pi}_J dA\end{aligned}\quad (59)$$

where \mathbf{K} is the global stiffness matrix expressed as

$$\mathbf{K} = \mathbf{K}_m + \mathbf{K}_G \quad (60)$$

Hence, to predict the geometrically nonlinear problem, the equilibrium equation can be written as

$$\mathbf{K} \Delta \boldsymbol{\Gamma} = \mathbf{F} \quad (61)$$

where \mathbf{F} combines either the internal and external work.

3. Numerical examples

In FEM, the integration mesh is coincident with the element mesh whereas in meshfree method, the structure is divided in regular grids forming quadrilateral integration cells known as the background cells. Numerical integration with 3×3 Gaussian quadrature on the background cells is considered for all the numerical examples with the present meshfree model. Using the RPIM approximation approach, the shape parameters c of the radial basis function is chosen optimally for each test whereas q is equal to 1.03 for all studied examples.

3.1 Cantilever plate

This test represents a cantilever plate subjected to an out-of-plane bending force $P = 10N$ applied in 10 load

steps, as shown in Fig. 2. The material properties of the cantilever plate are: The Young’s modulus $E = 1.2 \times 10^6$ N/mm² and the Poisson’s ratio $\nu = 0.3$. The geometry parameters are given as: length $L = 10$ mm, width $b = 1$ mm and thickness $h = 0.1$ mm. The deformed configuration of the cantilever plate is shown in Fig. 3.

For the meshfree method, the multiquadratic radial basis function approximation is chosen with a shape parameter c equal to 12 and a nodal distribution of 2×11 is adopted. Fig. 4 shows the load deflection of the cantilever plate. The present results are compared with those obtained by Li *et al.* (2018), using an isogeometric-meshfree coupling approach based on Kirchhoff-Love thin shell theory and the analytic solutions obtained by Timoshenko and Gere (1972). As seen in Fig. 4, the present results fairly agree with the analytical solutions and are good compared to the solutions of Li *et al.* (2018), since the load is limited in his work at $P = 4N$.

3.2 Clamped plate

This test represents a laminated composite square plate subjected to a uniform transverse load q_0 as shown in Fig. 5. The cross-ply laminates are considered $[0^\circ/90^\circ/90^\circ/0^\circ]$ and the material properties of each layer are the following

$$\begin{aligned}E_1 &= 1.8282 \times 10^6 \text{ psi}, & E_2 &= 1.8315 \times 10^6 \text{ psi}, \\ G_{12} &= G_{13} = 0.5E_2, & \nu_{12} &= 0.2395\end{aligned}$$

The geometrical properties are given as: length $a = 12in$, total thickness $h = 0.96in$ (4 layers), “The total number of nodes used in this test is 15×15 and the multiquadratic

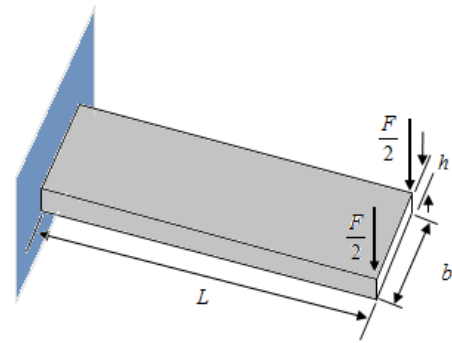


Fig. 2 The geometry of the cantilever plate

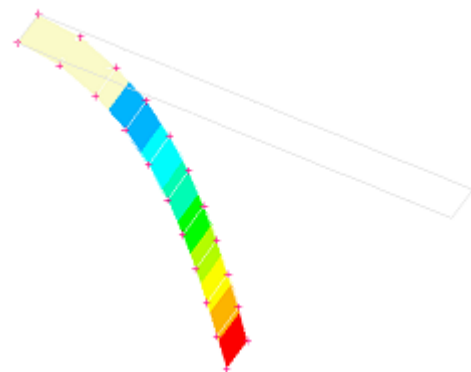


Fig. 3 Deformed configuration of the cantilever plate

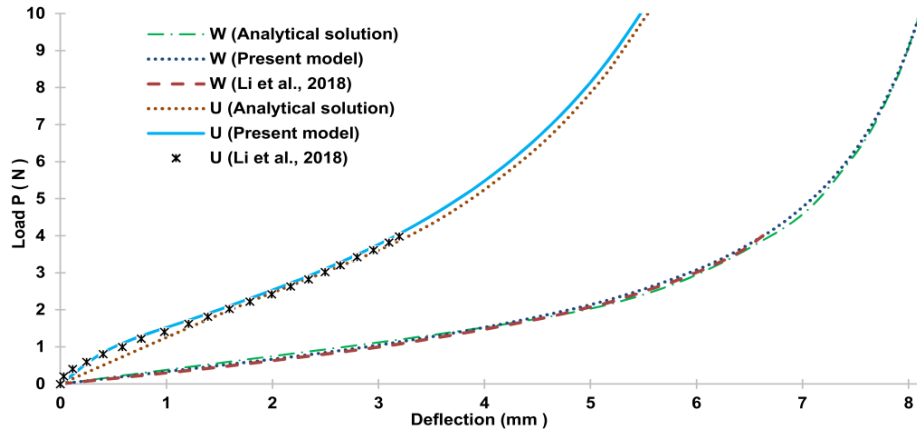


Fig. 4 The load deflection of the cantilever plate

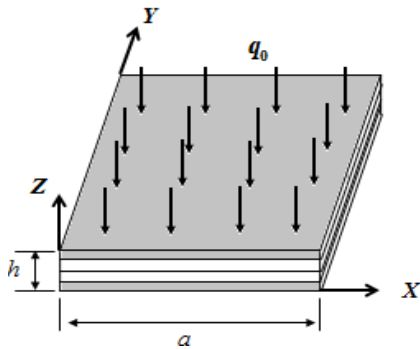


Fig. 5 The geometry of the clamped plate

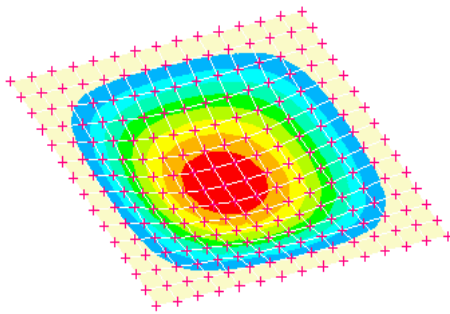


Fig. 6 Deformed configuration of the clamped plate

radial basis function is chosen with a shape parameter c equal to 1. The deformed configuration of the clamped plate is represented in Fig. 6.

The present results are compared with those obtained by Zhao *et al.* (2008). Fig. 7 shows centroidal deflection of the square plate under uniform load with the variation of the load. As seen in this figure, the present model gives good results compared to the reference results.

3.3 Pinched hemispherical shell with 18° hole

A hemispherical shell pierced with an 18° hole on the top and loaded by four concentrated radial forces (two inward and two outward) is presented in this section.

The analysis of the structure is reduced to a quadrant of the shell, since the symmetry of the problem, as shown in Fig. 8. Material and geometrical properties are given as: elastic modulus $E = 6.825 \times 10^7$ Pa, Poisson's ratio $\nu = 0.3$, thickness $h = 0.04$ mm, radius $R = 10$ mm and radial load $F = 400$ N. The radial basis function approximation used for this test is the Multiquadratic, where the shape parameter c is equal to 0.6 and a regular grid nodes 13×13 is performed. The undeformed and deformed configurations of the pinched hemispherical shell with 18° hole are shown in Fig. 9.

The performance of the present model is compared with the nonlinear DDSM of Frikha and Dammak (2017) and the

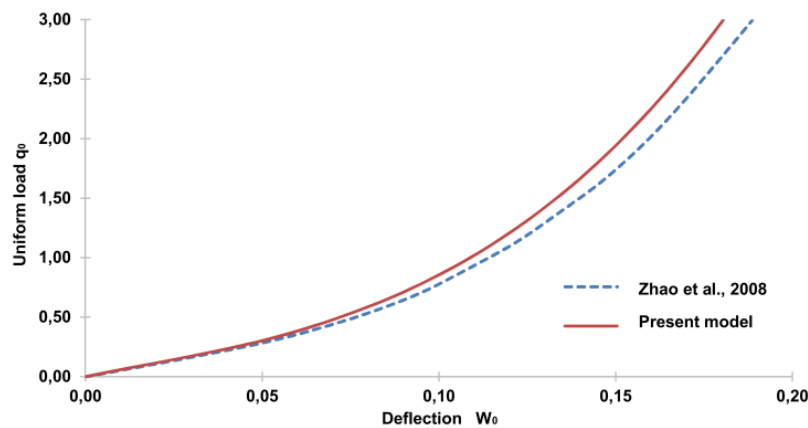


Fig. 7 Results of the clamped plate

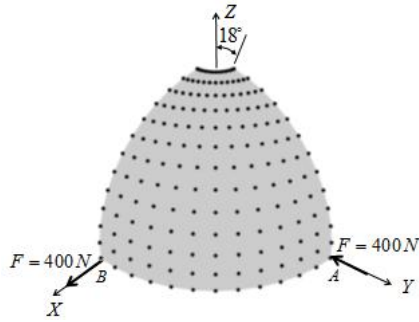


Fig. 8 Geometry of the pinched hemispherical shell with 18° hole

model of Li *et al.* (2018), using an isogeometric-meshfree coupling approach based on Kirchhoff-Love theory.

The results obtained by the present meshfree method (Fig. 10) fairly agree with the results of Frikha and Dammak (2017) and are good compared to the solutions of Li *et al.* (2018), demonstrating the accuracy of the DDSM applied with the present geometrically nonlinear meshfree approach.

3.4 Clamped cylindrical panel under concentrate transverse load

A clamped cylindrical shell panel under a concentrated transverse load $P = 7$ at the center point of the structure, as shown in Fig. 11, is examined in this part. The material and geometrical parameters of the cylindrical panel are given as: $E = 10^7$, $\nu = 0.3$, $L = 6$, $R = 2.5$, $h = 0.01$ and $\theta = 45^\circ$.



Fig. 9 The pinched hemispherical shell: (a) Undeformed configuration; (b) deformed configuration

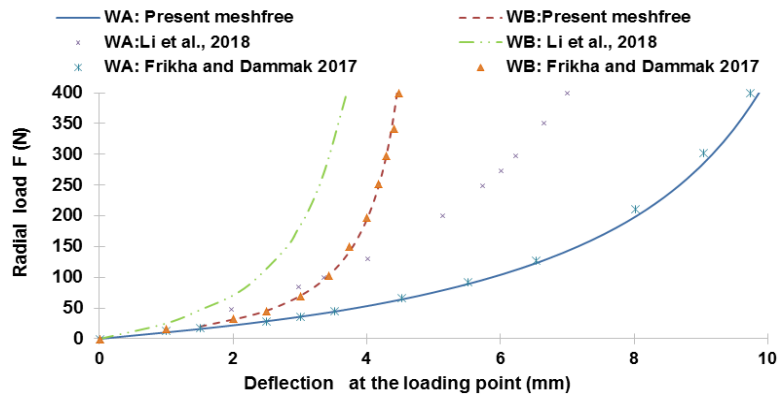


Fig. 10 The load-deflection curves at the points A and B of the hemispherical shell

A quarter of the structure is presented owing to the symmetry of the model. For the radial point interpolation method, the Gaussian radial basis function is chosen where the shape parameter c is equal to 5.1 with total nodes 11×13 . The deformed configuration of the clamped cylindrical panel is shown in Fig. 12.

The center point load-deflection is shown in Fig. 13 with comparison to the solutions of Frikha and Dammak (2017), using the nonlinear DDST and the results of Brendel and Ramm (1980), using an isoparametric large displacement shell model. The results obtained using the present model (Fig. 13) is consistent with the reference solutions.

It can be concluded from the results of Frikha and Dammak (2017), using the nonlinear DDST that the present meshfree method is accurate as the finite element one.

4. Conclusions

In this paper, a meshfree method is developed for the geometrically nonlinear analysis of 3D shell structures using the DDST. The RPIM is adopted to approximate the meshfree shape functions. The high accuracy and robustness of the developed model are evaluated through solutions of several non-trivial benchmark problems illustrated in the literature. Numerical examples have demonstrated that the present model provides accurate results for plates and shell structures since the meshfree methods depend only on distributed nodes in the problem domain. The proposed approach can be performed in

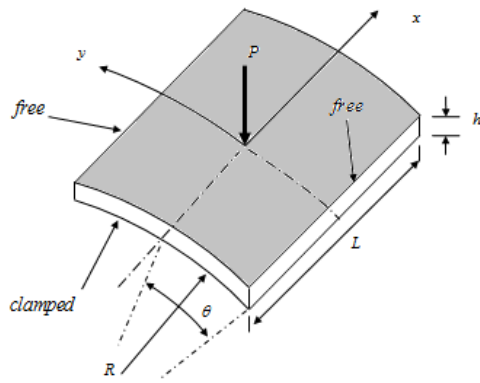


Fig. 11 Geometry of the clamped cylindrical panel

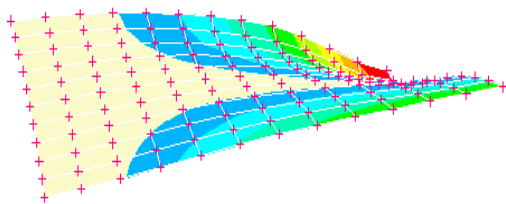


Fig. 12 The deformed configuration of the cylindrical panel

various mechanical behavior analysis such as the vibration and free vibration (Lei *et al.* 2015, Zhang *et al.* 2016b), the dynamic response (Lei *et al.* 2014, Zhang and Xiao 2017), and to study buckling and post-buckling effect (Zhang and Liew 2016, Zhang *et al.* 2016a, Zhang 2017, Trabelsi *et al.* 2019).

Acknowledgments

The authors extend their appreciation to the Deanship of Scientific Research at King Khalid University for funding this work through research groups program under grant number (R.G.P.1/68/40).

References

- Atri, H.R. and Shojaee, S. (2018), "Truncated hierarchical B-splines in isogeometric analysis of thin shell structures", *Steel Compos. Struct., Int. J.*, **26**(2), 171-182.
- Belinha, J. and Dinis, L.M.J.S. (2007), "Nonlinear analysis of plates and laminates using the element free Galerkin method", *Compos. Struct.*, **78**(3), 337-350.
- Brendel, B. and Ramm, E. (1980), "Linear and nonlinear stability analysis of cylindrical shells", *Comput. Struct.*, **12**(4), 549-558.
- Dinis, L.M.J.S., Jorge, R.N. and Belinha, J. (2008), "Analysis of plates and laminates using the natural neighbour radial point interpolation method", *Eng. Anal. Bound. Elem.*, **32**(3), 267-279.
- Ferreira, A.J.M., Roque, C.M.C. and Jorge, R.M.N. (2005), "Analysis of composite plates by trigonometric shear deformation theory and multiquadrics", *Comput. Struct.*, **83**(27), 2225-2237.
- Ferreira, A.J.M., Roque, C.M.C. and Jorge, R.M.N. (2006), "Static and free vibration analysis of composite shells by radial basis functions", *Eng. Anal. Bound. Elem.*, **30**(9), 719-733.
- Frikha, A. and Dammak, F. (2017), "Geometrically non-linear static analysis of functionally graded material shells with a discrete double directors shell element", *Comput. Methods Appl. Mech. Eng.*, **315**, 1-24.
- Ivannikov, V., Tiago, C. and Pimenta, P.D.M. (2014), "Meshless implementation of the geometrically exact Kirchhoff-Love shell theory", *Int. J. Numer. Methods Eng.*, **100**(1), 1-39.
- Jrad, H., Mallek, H., Wali, M. and Dammak, F. (2018a), "Finite element formulation for active functionally graded thin-walled structures", *Comptes Rendus Mecanique*, **346**(12), 1159-1178.
- Jrad, H., Mars, J., Wali, M. and Dammak, F. (2018b), "An extended finite element method for modeling elastoplastic FGM plate-shell type structures", *Struct. Eng. Mech., Int. J.*, **68**(3), 299-312.
- Jrad, H., Mars, J., Wali, M. and Dammak, F. (2018c), "Geometrically nonlinear analysis of elastoplastic behavior of functionally graded shells", *Eng. Comput.*, 1-15.
DOI: <https://doi.org/10.1007/s00366-018-0633-3>
- Kazemi, Z., Hematiyan, M.R. and Vaghefi, R. (2017), "Meshfree radial point interpolation method for analysis of viscoplastic problems", *Eng. Anal. Bound. Elem.*, **82**, 172-184.
- Kim, K.D., Lomboy, G.R. and Han, S.C. (2008), "Geometrically non-linear analysis of functionally graded material (FGM) plates and shells using a four-node quasi-conforming shell element", *J. Compos. Mater.*, **42**(5), 485-511.

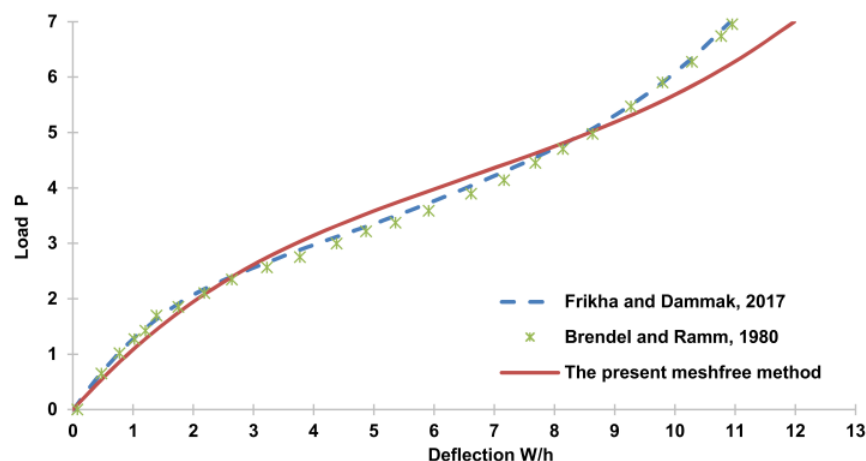


Fig. 13 The center point load-deflection of the clamped cylindrical panel

- Krysl, P. and Belytschko, T. (1996), "Analysis of thin shells by the element-free Galerkin method", *Int. J. Solids Struct.*, **33**(20-22), 3057-3080.
- Lei, Z. and Zhang, Y. (2018), "Characterizing buckling behavior of matrix-cracked hybrid plates containing CNTR-FG layers", *Steel Compos. Struct., Int. J.*, **28**(4), 495-508.
- Lei, Z.X., Zhang, L.W., Liew, K.M. and Yu, J.L. (2014), "Dynamic stability analysis of carbon nanotube-reinforced functionally graded cylindrical panels using the element-free kp-Ritz method", *Compos. Struct.*, **113**, 328-338.
- Lei, Z.X., Zhang, L.W. and Liew, K.M. (2015), "Free vibration analysis of laminated FG-CNT reinforced composite rectangular plates using the kp-Ritz method", *Compos. Struct.*, **127**, 245-259.
- Li, S.R., Fu, X.H. and Batra, R.C. (2010), "Free vibration of three-layer circular cylindrical shells with functionally graded middle layer", *Mech. Res. Commun.*, **37**(6), 577-580.
- Li, W., Nguyen-Thanh, N. and Zhou, K. (2018), "Geometrically nonlinear analysis of thin-shell structures based on an isogeometric-meshfree coupling approach", *Comput. Methods Appl. Mech. Eng.*, **336**, 111-134.
- Liew, K.M., Wang, J., Tan, M.J. and Rajendran, S. (2004), "Nonlinear analysis of laminated composite plates using the mesh-free kp-Ritz method based on FSDT", *Comput. Methods Appl. Mech. Eng.*, **193**(45-47), 4763-4779.
- Liew, K.M., Peng, L.X. and Kitipornchai, S. (2007), "Nonlinear analysis of corrugated plates using a FSDT and a meshfree method", *Comput. Methods Appl. Mech. Eng.*, **196**(21-24), 2358-2376.
- Liew, K.M., Zhao, X. and Ferreira, A.J. (2011), "A review of meshless methods for laminated and functionally graded plates and shells", *Compos. Struct.*, **93**(8), 2031-2041.
- Liu, G.R. and Gu, Y.T. (2005), *An Introduction to Meshfree Methods and their Programming*, Springer Science & Business Media.
- Mallek, H., Jrad, H., Algahtani, A., Wali, M. and Dammak, F. (2019a), "Geometrically non-linear analysis of FG-CNTRC shell structures with surface-bonded piezoelectric layers", *Comput. Methods Appl. Mech. Eng.*, **347**, 679-699.
- Mallek, H., Jrad, H., Wali, M. and Dammak, F. (2019b), "Geometrically nonlinear finite element simulation of smart laminated shells using a modified first-order shear deformation theory", *J. Intel. Mater. Syst. Struct.*, **30**(4), 517-535.
- Mallek, H., Jrad, H., Wali, M. and Dammak, F. (2019c), "Piezoelectric response of smart functionally graded structure with integrated piezoelectric layers using discrete double directors shell element", *Compos. Struct.*, **210**, 354-366.
- Marinković, D. and Rama, G. (2017), "Co-rotational shell element for numerical analysis of laminated piezoelectric composite structures", *Compos. Part B: Eng.*, **125**, 144-156.
- Mellouli, H., Jrad, H., Wali, M. and Dammak, F. (2019a), "Meshfree implementation of the double director shell model for FGM shell structures analysis", *Eng. Anal. Bound. Elem.*, **99**, 111-121.
- Mellouli, H., Jrad, H., Wali, M. and Dammak, F. (2019b), "Meshless implementation of arbitrary 3D-shell structures based on a modified first order shear deformation theory", *Comput. Math. Appl.*, **77**, 34-49.
- Nguyen, T.N., Thai, C.H., Nguyen-Xuan, H. and Lee, J. (2018), "Geometrically nonlinear analysis of functionally graded material plates using an improved moving Kriging meshfree method based on a refined plate theory", *Compos. Struct.*, **193**, 268-280.
- Noguchi, H., Kawashima, T. and Miyamura, T. (2000), "Element free analyses of shell and spatial structures", *International J. Numer. Methods Eng.*, **47**(6), 1215-1240.
- Qian, L.F., Batra, R.C. and Chen, L.M. (2003), "Elastostatic deformations of a thick plate by using a higher-order shear and normal deformable plate theory and two meshless local Petrov-Galerkin (MLPG) methods", *Comput. Model. Eng. Sci.*, **4**(1), 161-176.
- Qian, L.F., Batra, R.C. and Chen, L.M. (2004), "Analysis of cylindrical bending thermoelastic deformations of functionally graded plates by a meshless local Petrov-Galerkin method", *Computat. Mech.*, **33**(4), 263-273.
- Rama, G. (2017), "A 3-node piezoelectric shell element for linear and geometrically nonlinear dynamic analysis of smart structures", *Facta Universitatis, Series: Mechanical Engineering*, **15**(1), 31-44.
- Rama, G., Marinković, D. and Zehn, M. (2018), "Efficient three-node finite shell element for linear and geometrically nonlinear analyses of piezoelectric laminated structures", *J. Intel. Mater. Syst. Struct.*, **29**(3), 345-357.
- Ray, M.C. and Batra, R.C. (2008), "Smart constrained layer damping of functionally graded shells using vertically/obliquely reinforced 1-3 piezocomposite under a thermal environment", *Smart Mater. Struct.*, **17**(5), 055007.
- Rezaiee Pajand, M., Masoodi, A. and Arabi, E. (2018), "Geometrically nonlinear analysis of FG doubly-curved and hyperbolic shells via laminated by new element", *Steel Compos. Struct., Int. J.*, **28**(3), 389-401.
- Sladek, J., Sladek, V., Krivacek, J., Wen, P.H. and Zhang, C. (2007), "Meshless local Petrov-Galerkin (MLPG) method for Reissner-Mindlin plates under dynamic load", *Comput. Methods Appl. Mech. Eng.*, **196**(25-28), 2681-2691.
- Tiago, C. and Pimenta, P.M. (2008), "An EFG method for the nonlinear analysis of plates undergoing arbitrarily large deformations", *Eng. Anal. Bound. Elem.*, **32**(6), 494-511.
- Timoshenko, S.P. and Gere, J.M. (1972), *Mechanics of Materials*, van Nostrand Reinhold Company, New York, NY, USA.
- Trabelsi, S., Frikha, A., Zghal, S. and Dammak, F. (2019), "A modified FSDT-based four nodes finite shell element for thermal buckling analysis of functionally graded plates and cylindrical shells", *Eng. Struct.*, **178**, 444-459.
- Uysal, M.U. (2016), "Buckling behaviours of functionally graded polymeric thin-walled hemispherical shells", *Steel Compos. Struct., Int. J.*, **21**(4), 849-862.
- Vu, T.V., Khosravifard, A., Hematiyan, M.R. and Bui, T.Q. (2018), "A new refined simple TSDT-based effective meshfree method for analysis of through-thickness FG plates", *Appl. Math. Model.*, **57**, 514-534.
- Wali, M., Hajlaoui, A. and Dammak, F. (2014), "Discrete double directors shell element for the functionally graded material shell structures analysis", *Comput. Methods Appl. Mech. Eng.*, **278**, 388-403.
- Wang, J.G. and Liu, G.R. (2002), "On the optimal shape parameters of radial basis functions used for 2-D meshless methods", *Comput. Methods Appl. Mech. Eng.*, **191**(23-24), 2611-2630.
- Wu, C.P. and Liu, Y.C. (2016), "A state space meshless method for the 3D analysis of FGM axisymmetric circular plates", *Steel Compos. Struct., Int. J.*, **22**(1), 161-182.
- Zghal, S., Frikha, A. and Dammak, F. (2017), "Static analysis of functionally graded carbon nanotube-reinforced plate and shell structures", *Compos. Struct.*, **176**, 1107-1123.
- Zhang, L.W. (2017), "An element-free based IMLS-Ritz method for buckling analysis of nanocomposite plates of polygonal planform", *Eng. Anal. Bound. Elem.*, **77**, 10-25.
- Zhang, L.W. and Liew, K.M. (2016a), "Element-free geometrically nonlinear analysis of quadrilateral functionally graded material plates with internal column supports", *Compos. Struct.*, **147**, 99-110.
- Zhang, L.W. and Liew, K.M. (2016b), "Postbuckling analysis of axially compressed CNT reinforced functionally graded

- composite plates resting on Pasternak foundations using an element-free approach”, *Compos. Struct.*, **138**, 40-51.
- Zhang, L.W. and Xiao, L.N. (2017), “Mechanical behavior of laminated CNT-reinforced composite skew plates subjected to dynamic loading”, *Compos. Part B: Eng.*, **122**, 219-230.
- Zhang, L.W., Cui, W.C. and Liew, K.M. (2015a), “Vibration analysis of functionally graded carbon nanotube reinforced composite thick plates with elastically restrained edges”, *Int. J. Mech. Sci.*, **103**, 9-21.
- Zhang, L.W., Lei, Z.X. and Liew, K.M. (2015b), “Buckling analysis of FG-CNT reinforced composite thick skew plates using an element-free approach”, *Compos. Part B: Eng.*, **75**, 36-46.
- Zhang, L.W., Song, Z.G. and Liew, K.M. (2015c), “Nonlinear bending analysis of FG-CNT reinforced composite thick plates resting on Pasternak foundations using the element-free IMLS-Ritz method”, *Compos. Struct.*, **128**, 165-175.
- Zhang, L.W., Liew, K.M. and Reddy, J.N. (2016a), “Postbuckling behavior of bi-axially compressed arbitrarily straight-sided quadrilateral functionally graded material plates”, *Comput. Methods Appl. Mech. Eng.*, **300**, 593-610.
- Zhang, L.W., Zhang, Y., Zou, G.L. and Liew, K.M. (2016b), “Free vibration analysis of triangular CNT-reinforced composite plates subjected to in-plane stresses using FSDT element-free method”, *Compos. Struct.*, **149**, 247-260.
- Zhao, X., Liu, G.R., Dai, K.Y., Zhong, Z.H., Li, G.Y. and Han, X. (2008), “Geometric nonlinear analysis of plates and cylindrical shells via a linearly conforming radial point interpolation method”, *Computat. Mech.*, **42**(1), 133-144.
- Zhu, P., Zhang, L.W. and Liew, K.M. (2014), “Geometrically nonlinear thermomechanical analysis of moderately thick functionally graded plates using a local Petrov–Galerkin approach with moving Kriging interpolation”, *Compos. Struct.*, **107**, 298-314.

CC

Appendix A: Geometrical tangent matrix

For a couple of nodes (i, j), the matrix \mathbf{K}_G is expressed as

$$\mathbf{K}_{G_{ij}} = \begin{bmatrix} UUM_{ij}\mathbf{I} & (UBF_{1ij} + UBC_{1ij})\mathbf{I} & (UBF_{2ij} + UBC_{2ij})\mathbf{I} \\ (BUF_{1ij} + BUC_{1ij})\mathbf{I} & (BBF_{1ij} + BBC_{1ij})\mathbf{I} & \mathbf{0} \\ (BUF_{2ij} + BUC_{2ij})\mathbf{I} & \mathbf{0} & (BBF_{2ij} + BBC_{2ij})\mathbf{I} \end{bmatrix} \quad (\text{A1})$$

Where UUM , $(UBF_1, BBF_1, UBF_2, BBF_2)$ and $(UBC_1, BBC_1, UBC_2, BBC_2)$ corresponding to membrane, bending and shear components respectively. The expression of membrane term is written as

$$UUM_{ij} = \int (\varphi_1^i (N^{11} \varphi_1^j + N^{12} \varphi_2^j) + \varphi_2^i (N^{12} \varphi_1^j + N^{22} \varphi_2^j)) dA \quad (\text{A2})$$

The bending terms of the first director vector \mathbf{d}_1 are given by

$$UBF_{1ij} = \int (\varphi_1^i (M_1^{11} \varphi_1^j + M_1^{12} \varphi_2^j) + \varphi_2^i (M_1^{12} \varphi_1^j + M_1^{22} \varphi_2^j)) dA \quad (\text{A3})$$

$$BBF_{1ii} = - \int (\varphi_1^i ((\mathbf{a}_1 \cdot \mathbf{d}_{1i}) M_1^{11} + (\mathbf{a}_2 \cdot \mathbf{d}_{1i}) M_1^{12}) + \varphi_2^i ((\mathbf{a}_1 \cdot \mathbf{d}_{1i}) M_1^{12} + (\mathbf{a}_2 \cdot \mathbf{d}_{1i}) M_1^{22})) dA \quad (\text{A4})$$

$$BBF_{1ij} = 0, \quad i \neq j; \quad BUF_{1ij} = UBF_{1ij} \quad (\text{A5})$$

The bending terms of the second director vector \mathbf{d}_2 are expressed as

$$UBF_{2ij} = \int (\varphi_1^i (M_2^{11} \varphi_1^j + M_2^{12} \varphi_2^j) + \varphi_2^i (M_2^{12} \varphi_1^j + M_2^{22} \varphi_2^j)) dA \quad (\text{A6})$$

$$BBF_{2ii} = - \int (\varphi_1^i ((\mathbf{a}_1 \cdot \mathbf{d}_{2i}) M_2^{11} + (\mathbf{a}_2 \cdot \mathbf{d}_{2i}) M_2^{12}) + \varphi_2^i ((\mathbf{a}_1 \cdot \mathbf{d}_{2i}) M_2^{12} + (\mathbf{a}_2 \cdot \mathbf{d}_{2i}) M_2^{22})) dA \quad (\text{A7})$$

$$BBF_{2ij} = 0, \quad i \neq j; \quad BUF_{2ij} = UBF_{2ij} \quad (\text{A8})$$

The transverse shear terms of the first director vector \mathbf{d}_1 are given by

$$UBC_{1ij} = \int (\varphi_1^i T_1^1 \varphi_1^j + \varphi_2^i T_2^1 \varphi_1^j) dA \quad (\text{A9})$$

$$BBC_{1ii} = - \int (\varphi_1^i (\mathbf{a}_1 \cdot \mathbf{d}_{1i}) T_1^1 + \varphi_2^i (\mathbf{a}_2 \cdot \mathbf{d}_{1i}) T_2^1) dA \quad (\text{A10})$$

$$BBC_{1ij} = 0, \quad i \neq j; \quad BUC_{1ij} = UBC_{1ij} \quad (\text{A11})$$

The transverse shear terms of the second director vector \mathbf{d}_2 are expressed as

$$UBC_{2ij} = \int (\varphi_1^i T_1^2 \varphi_1^j + \varphi_2^i T_2^2 \varphi_1^j) dA \quad (\text{A12})$$

$$BBC_{2ii} = - \int (\varphi_1^i (\mathbf{a}_1 \cdot \mathbf{d}_{2i}) T_1^2 + \varphi_2^i (\mathbf{a}_2 \cdot \mathbf{d}_{2i}) T_2^2) dA \quad (\text{A13})$$

$$BBC_{2ij} = 0, \quad i \neq j; \quad BUC_{2ij} = UBC_{2ij} \quad (\text{A14})$$